Publications of the Astronomical Society of the Pacific, 135:084103 (14pp), 2023 August https://doi.org/10.1088/1538-3873/acf074

Comparison Between TeV and Non-TeV Fermi-detected BL Lacertae Objects

Jingchao Liang[1,2,3], Xiangtao Zeng[1,2,3], Guohai Chen[1,2,3], Xuhong Ye[4], Jingtian Zhu[1,2,3,4], Hubing Xiao[5], Zhiyuan Pei[1,2,3], Guangjie Du[6], Gao Ying[6], and Junhui Fan[1,2,3,7]

[1] Center for Astrophysics, Guangzhou University Guangzhou, 510006, People's Republic of China; fjh@gzhu.edu.cn
[2] Astronomy Science and Technology Research Laboratory of Department of Education of Guangdong Province, Guangzhou 510006, People's Republic of China
[3] Key Laboratory for Astronomical Observation and Technology of Guangzhou, Guangzhou 510006, People's Republic of China
[4] Department of Physics and Astronomy "G. Galilei,"University of Padova, Padova I-35131, Italy
[5] Shanghai Key Lab for Astrophysics, Shanghai Normal University Shanghai, 200234, People's Republic of China
[6] School of Physics and Materials Science, Guangzhou University, Guangzhou, 510006, People's Republic of China
Received 2023 April 18; accepted 2023 August 15; published 2023 August 31

Abstract

In this paper, we compiled a sample of 410 Fermi-detected BL Lacs, including 42 TeV-detected BL Lacs (TBLs) and 368 non-TeV-detected BL Lacs (non-TBLs) with corresponding mid-infrared (mid-IR), TeV and Fermi γ-ray data, and calculated some important parameters including monochromatic luminosities (mid-IR, GeV and TeV bands) and mid-IR spectral indices. Based on those parameters, we discussed the relationship between the mid-IR and the TeV bands and that between the mid-IR and the GeV bands. Main conclusions are drawn as follows: (1) In the color–color and color–magnitude diagrams, our sample forms a WISE-Gamma Strip in the [3.4]–[4.6]–[12] μm color–color diagram, and TBLs occupy the brighter region than the non-TBLs for the similar color-index in the color-magnititue diagram; (2) The mid-IR luminosity of the TBLs is on average higher than that of non-TBLs, while the average mid-IR spectral index of TBLs is smaller than the non-TBLs, suggesting that TBLs are brighter and hold a more flat spectrum than do the non-TBLs in the mid-IR band. Besides, HBLs have a more flat mid-IR spectrum than LBLs and IBLs; (3) The mid-IR luminosity is positively correlated with the GeV luminosity and the intrinsic TeV luminosity. A positive correlation exists between the mid-IR spectral index and the observed TeV spectral index, which is consistent with the expectations of the synchrotron self-Compton mechanism. We suggest that the HBLs with extreme relativistic electrons might scatter the mid-IR photons up to the TeV band.

Unified Astronomy Thesaurus concepts: Active galactic nuclei (16); Blazars (164); BL Lacertae objects (158); Gamma-rays (637)

1. Introduction

Blazars are the most powerful active galactic nucleus (AGNs) with extreme observational properties, such as high luminosity, high and varible polarization, rapid variability from radio even up to TeV region, superluminal motions, core-dominated nonthermal continuum, or strong γ-ray emissions etc. Those extreme properties are due to the relativistic jets pointing at a small viewing angle (<10°) toward the observer (Blandford & Rees 1978; Wills et al. 1992; Urry & Padovani 1995; Chen & Shan 2011; Massaro et al. 2011; Fan et al. 2012, 2016; Padovani et al. 2017; Xiao et al. 2019; Abdollahi et al. 2020; Zhang et al. 2020; Fan et al. 2021; Ye et al. 2021; Zhang et al. 2022a; Yang et al. 2022b; Abdollahi et al. 2022; Cai et al. 2022; Pei et al. 2022; Prandini & Ghisellini 2022; Xiao et al. 2022; Zeng et al. 2022). Based on the observational features, blazars can be grouped as two subclass: BL Lacertae objects (BL Lacs) and flat spectrum radio quasars (FSRQs). BL Lacs are characterized by weak or even absent emission lines, while FSRQs exhibit the usual quasar-like broad emission line. The typical spectral energy distribution (SED) of the blazars is characterized by two broad bumps (Fossati et al. 1998), where the low-energy bump is thought to be produced by the synchrotron process while the high-energy bump, in a leptonic model, is produced by inverse Compton scattering. Based on the peak frequency ($\log \nu_p^s$) for the synchrotron component, blazars can be further classified into low synchrotron peaked (LSP) blazars with $\log \nu_p^s < 14$ Hz, intermediate synchrotron peaked (ISP) blazars with 14 Hz $< \log \nu_p^s <$ 15 Hz, and high synchrotron peaked (HSP) blazars with $\log \nu_p^s >$ 15 Hz (Abdo et al. 2010). Later on Fan et al. (2016) adopted the acronyms to the analysis of the logarithm of the synchrotron peak frequencies for 1392 Fermi blazars and proposed a classification boundary, which is 14.0 and 15.3 Hz, namely $\log \nu_p^s <$ 14.0 Hz for LSPs, 14.0 Hz $< \log \nu_p^s <$ 15.3 Hz for ISPs and $\log \nu_p^s >$ 15.3 Hz for HSPs. The classification was also revisited in a recent work by Yang et al. (2022a) who calculated the SEDs for 2709 fermi-detected blazars and suggested separating them with

[7] Corresponding author.

synchrotron peak frequency: $\log \nu_p^s < 13.7$ for LSPs, $13.7\ \mathrm{Hz} < \log \nu_p^s < 14.9\ \mathrm{Hz}$ for ISPs and $\log \nu_p^s > 14.9\ \mathrm{Hz}$ for HSPs. The corresponding types for BL Lacs are named LBLs, IBLs and HBLs, respectively.It seems that the classifications of 3 components (LSP, ISP and HSP) are effextively the same in these works (Abdo et al. 2010; Fan et al. 2016; Yang et al. 2022a) but the boundary peak frequencies differ slightly in different works.

Since the launch of Fermi-LAT satellite, our knowledge about GeV γ-ray AGNs has been revolutionized (Abdo et al. 2009; Atwood et al. 2009; Ackermann et al. 2011). In particularly, the γ-ray detections in blazars provide us with a valuable opportunity to explore the γ-ray mechanism. According to the lepton scenario, the high energy is produced by inverse Compton scattering, and the scattered photons may come from synchrotron radiation, i.e., the synchrotron self-Compton (SSC) (Konigl 1981; Marscher & Gear 1985; Ghisellini & Maraschi 1989), or external to the jet, namely the external Compton process (EC) (Begelman & Sikora 1987; Melia & Konigl 1989). Besides, the γ-ray emission can also be produced by various hadronic models, e.g., the γ-ray emission is produced by accelerated protons interacting with ambient gas or low-frequency radiation (Aharonian 2000; Deng et al. 2022). One can provide important insights into the soft photons inducing the observed γ-ray by exploring the correlation between the γ-ray emission and the low-energy (radio to X-ray) emission (Ghisellini & Maraschi 1989; Dondi & Ghisellini 1995; Xie et al. 1997; Zhang & Xie 1997; Fan et al. 1998; Ackermann et al. 2011; Liodakis et al. 2018).

The NASA Wide-field Infrared Survey Explorer (WISE) completed a mid-infrared survey of the entire sky in 2010. WISE mission mapped the sky at 3.4 μm (W1), 4.6 μm (W2), 12 μm (W3), and 22 μm (W4) with an angular resolution of $6\farcs1$, $6\farcs4$, $6\farcs5$ and $12\farcs0$ respectively, achieving 5σ point source sensitivities of 0.08 mJy, 0.11 mJy, 1 mJy, and 6 mJy in unconfused regions on the ecliptic, which makes it possible to conduct the statistical investigation in the mid-IR for blazars (Wright et al. 2010). Since the stellar photospheric contributions do not dominate galaxy colors in the mid-IR, blazars are distributed in a distinct region separated from other extragalactic sources in the mid-IR in the [3.4]–[4.6] μm against [4.6]–[12] μm colorcolor diagram, which is called the WISE Blazars Strip (WBS), and the γ-ray-emitting blazars also occupy a distinct region diagrams, also known as the WISE Gamma-ray Strip (WGS) (Massaro et al. 2011; D'Abrusco et al. 2012). Observations in the IR band not only help us to obtain direct information on their underlying continua and emission mechanisms, but also provide deeper insight into the contributions of the jet, torus, and host galaxy (Falomo et al. 1993; Pian et al. 1994; Chen et al. 2005; Hardcastle et al. 2009; Plotkin et al. 2012; Anjum et al. 2020).

On very high energies (i.e., E $\geqslant$ 100 GeV), BL Lac objects, in particular HBLs, constitute the biggest known TeV extragalactic source population detected by ground-based Cherenkov telescopes, e.g., the Major Atmospheric Gamma-ray Imaging Cherenkov Telescopes (MAGIC), the High Energy Stereoscopic System (H.E.S.S.), the Very Energetic Radiation Imaging Telescope Array System (VERITAS), and the Large High Altitude Air Shower Observatory (LHAASO). There are still many open questions about VHE, e.g., the origin of VHE emission, the mechanism of particle acceleration and the selection of TeV emission candidates. Being the most numerous extragalactic sources known to emit at these energies, TeV observations of BL Lacs are particularly noteworthy. Given that the necessity of high energy electrons and abundant seed photons to generate TeV emissions, BL Lacs are the best candidates on account of BL Lacs having their synchrotron peak located at high energies together with the sufficient radio-optical flux (Costamante & Ghisellini 2002). Massaro et al. (2011), Massaro et al. (2013) mentioned that the region of the WGS covered by the TBLs is well defined. The WISE data can thus be used to identify new TeV candidates, and the WGS can also be used as a diagnostic tool to classify blazars as well as unidentified γ-ray sources (Massaro et al. 2012; D'Abrusco et al. 2014, 2019); Lin & Fan (2016) compared multi-band observations of TBLs and non-TBLs, but did not involve the IR band. Among the findings, we are not only motivated to investigate the IR-γ relationship using WISE data for exploring the high-energy radiation mechanism, but also prompted to investigate whether there is a difference between TBLs and non-TBLs in the mid-IR band.

In this paper, we refer to the BL Lacs detected at TeV energy as TBLs and no TeV detection as non-TBLs. We aim to study the correlation between the mid-IR and GeV/TeV, and to explore the different behaviors for TBLs and non-TBLs. This paper is arranged as follows: Section 2 describes the sample and data process; Section 3 gives the results; we then conduct the discussions in Section 4 and Section 5 will summarize our conclusions. The cosmological parameters $H_0 = 67.4$ km s^{-1} Mpc^{-1}, $\Omega_m = 0.315$ and $\Omega_\Lambda = 0.69$ are adopted through this paper (Planck Collaboration et al. 2020).

2. Sample and Data Process

2.1. Sample

To investigate the correlation between the γ-ray and the mid-IR bands for BL Lacs, we focus on extragalactic survey regions with γ-ray observations and mid-IR observations from Fermi-LAT and WISE, respectively. We extract 1236 BL Lacs from the fourth catalog of active galactic nuclei (AGNs) detected by the Fermi Large Area Telescope (4LAC-DR2) (Abdollahi et al. 2020, 2022) and collect available redshift, SED classification (based on the synchrotron peak frequency), γ-ray flux (F_γ) at 1100 GeV, and the corresponding γ-ray photon index (Γ_{GeV}).

We adopt the synchrotron peak frequency classification criterion for the BL Lacs for the FermiWISE blazars sample to distinguish LBLs, IBLs and HBLs according to latest 4LAC catalog (Ajello et al. 2022). If a source has no available synchrotron peak frequency in 4LAC, we refer to Yang et al. (Yang et al. 2023). As for the TeV band, we collected energy spectrum information through TeV-emitting γ-ray sources catalog (TeVCat[8]) and available references.

By combining data from the WISE cryogenic and NEOWISER[9] (Mainzer et al. 2011) post-cryogenic survey phases, the AllWISE[10] catalog forms the most comprehensive view of the full mid-infrared sky currently available. Adopting the statistical criterion described in previous works (Massaro et al. 2011; D'Abrusco et al. 2012), we cross-matched our sample with a search radius of 2$''$.4 in AllWISE catalog (Massaro et al. 2011; Anjum et al. 2020), and excluded multiple cross-matches. Only sources with a signal-to-noise ratio (S/N) above 7 in the mid-IR bands are considered. Giving the high detection rate of Fermi blazars by the first three filters of WISE, we focus on the analysis on 3.4 μm, 4.6 μm, and 12 μm. To avoid any differences introduced by the redshift (either as a direct result of galaxy evolution or selection bias), only are the non-TBLs whose redshift falls in the redshift coverage of TBLs are considered here. In this sense, we obtained a sample of 410 Fermi BL Lacs with corresponding WISE counterpart, which we refer as subset A1, which include 42 TBLs (subset T1) and 368 non-TBLs (subset N1). The redshift ranges from $z = 3.70\text{E-}05$ (4FGL J0719.7-4012) to $z = 0.62$ (4FGL J0314.3+0620) for the whole sample. It is appropriate to restrict to $z \sim 0.6$, as TeV blazars detected at further distances are usually during flares. The remaining sources have no obvious counterpart in the 2$''$.4 range of WISE sources, but using a search radius of 12$''$ can be associated but without taking into account.

The corresponding data are listed in Table 1 and the redshift distribution is shown in Figure 1.

2.2. Data Process

The reported WISE magnitudes are converted to flux densities using zero-magnitude flux densities

$$f_\nu = f_0 10^{-0.4m} (Jy) \tag{1}$$

where m represents the magnitude, and f_0 is the zero-magnitude flux density, i.e., $f_0 = 306.681$ Jy, 170.66 Jy and 29.04 Jy for the W1, W2 and W3 bands respectively (Wright et al. 2010). As many authors have pointed out the infrared spectrum of BL Lacs is dominated by non-thermal radiation and can be described as a power-law spectrum with an index α, i.e., $f_\nu \propto \nu^{-\alpha}$ (Blandford & Rees 1978; Impey et al. 1982; Falomo et al. 1993; Pian et al. 1994), which follows $\log f_\nu = -\alpha \log \nu + b$. Then, the mid-IR spectral index $\alpha_{\rm MIR}$ can be derived between 3.4 and 12 μm bands and shown in the column (10) in Table 1 and the corresponding distribution is shown in Figure 2. It is known that the absorption of the galaxy at WISE wavelengths is negligible, hence in this work, we did not make the galaxy absorption corrections (Massaro et al. 2011).

The γ-ray photon flux follows a power-law spectrum model (Fan 2000; Acero et al. 2015; Singal 2015), and the observed photons can be converted to flux densities. Let

$$\frac{dN}{dE} = N_0 \cdot \left(\frac{E}{\mathrm{E}_0}\right)^{(-\Gamma_{\rm GeV})}, \tag{2}$$

where N is the observed integral γ-ray photon flux in units of photons cm^{-2} s^{-1}, N_0 is a constant and E_0 is the threshold energy, which need to be specified with the proper units. For the GeV energy band, N_0 can be calculated by

$$N_0 = N \cdot \frac{1 - \Gamma_{\rm GeV}}{E_U^{1-\Gamma_{\rm GeV}} - E_L^{1-\Gamma_{\rm GeV}}}, \tag{3}$$

where E_L and E_U are taken the values of 1 GeV and 100 GeV, respectively.

Since the observed VHE spectrum is attenuated by the EBL, we therefore need to obtain the absorption corrected spectrum by using the following equation,

$$\frac{dN}{dE_{\rm int}} = \frac{dN}{dE_{\rm obs}} e^{\tau_{\gamma\gamma}(E,z)}, \tag{4}$$

where $\tau_{\gamma\gamma}$ (E, z) is the EBL absorption depth of a photon at energy E from a source at redshift z. We employed the semi-analytic modeling (SAMs) of the EBL proposed by Gilmore et al. (2012), which predicted the evolving EBL and γ-ray opacity in the SAMs.

The flux density can be calculated by formula $f(E) = \frac{dF}{dE}$, where $dF = EdN$. Thus, for the GeV band, we can get

$$f(E) = N_0 \cdot \left(\frac{E}{E_0}\right)^{1-\Gamma_{\rm GeV}} (\text{GeV cm}^{-2}\text{ s}^{-1}\text{ GeV}^{-1}), \tag{5}$$

For the TeV band, considering the incomplete energy spectrum information of some sources, we adopt two calculation methods. Sources with complete energy spectrum information, the flux density at E TeV can be obtained by

$$f(E) = N_0 \cdot \left(\frac{E}{E_0}\right)^{1-\Gamma_{\rm TeV}} (\text{TeV cm}^{-2}\text{ s}^{-1}\text{ TeV}^{-1}), \tag{6}$$

where $\Gamma_{\rm TeV}$ is the TeV spectral index. The TeV flux usually in crab units, according to Aharonian et al. (2006) and Zhang et al. (2022b), the flux density of k crab can also be expressed as

$$f(E) = I_0 \cdot \left(\frac{E}{\rm TeV}\right)^{(1-\alpha_{\rm crab})} \cdot k (\text{TeV cm}^{-2}\text{ s}^{-1}\text{ TeV}^{-1}), \tag{7}$$

[8] http://tevcat.uchicago.edu/
[9] http://wise2.ipac.caltech.edu/docs/release/neowise//
[10] http://wise2.ipac.caltech.edu/docs/release/allwise//

Table 1
Sample of TeV BL Lacs

4FGL Name	Other Name	z	log ν_p^s	$\Gamma_{\rm TeV}^{\rm obs}$	$\Gamma_{\rm TeV}^{\rm int}$	$\Gamma_{\rm GeV}$	$\alpha_{\rm MIR}$	log $\nu L_{\rm TeV}^{\rm obs}$	log $\nu L_{\rm TeV}^{\rm int}$	log $\nu L_{\rm GeV}$	log $\nu L_{3.4}$	log $\nu L_{4.6}$	log νL_{12}	References
(1)	(2)	(3)	(4)	(5)	(6)	(7)	(8)	(9)	(10)	(11)	(12)	(13)	(14)	(15)
4FGL J1104.4+3812	MKN 421	0.031	16.22	2.35	2.74	1.78	−0.12	44.67	44.81	44.41	44.03	43.90	43.42	Albert et al. (2007a)
4FGL J1653.8+3945	MKN 501	0.034	15.45	2.72	2.28	1.79	−0.05	43.45	43.58	43.95	43.95	43.75	43.35	Acciari et al. (2011)
4FGL J2347.0+5141	1ES 2344+514	0.044	16.60	2.46	2.20	1.81	−0.33	43.28	43.46	43.59	43.69	43.44	42.94	Allen et al. (2017)
4FGL J1136.4+7009	MKN 180	0.045	17.48	3.3	2.91	1.73	−0.06	43.41	43.59	42.93	43.67	43.44	43.06	Albert et al. (2006a)
4FGL J2000.0+6508	1ES 1959+650	0.048	15.96	2.72	2.25	1.82	2.03E-03	43.64	43.86	44.18	43.85	43.72	43.30	Albert et al. (2006b)
4FGL J0214.3+5145	TXS 0210+515	0.049	15.90	2	1.65	1.89	−0.29	42.21	42.43	42.78	43.57	43.32	42.84	Acciari et al. (2020)
4FGL J2202.7+4216	BL Lacertae	0.069	13.59	3.6		2.18	0.90	43.29	43.61	42.38	45.06	45.07	45.01	Albert et al. (2007b)
4FGL J2009.4-4849	PKS 2005-489	0.071	15.30	3.2	2.71	1.84	0.25	43.65	43.97	42.56	44.46	44.37	44.05	H.E.S.S. Collaboration et al. (2010a)
4FGL J1744.0+1935	1ES 1741+196	0.084	17.24	2.4	2.36	1.95	−0.11	43.48	43.86	43.44	44.01	43.81	43.39	Ahnen et al. (2017)
4FGL J1221.5+2814	W Comae	0.103	14.65	3.68	2.38	2.15	0.43	43.71	44.18	43.99	44.61	44.56	44.30	Acciari et al. 2009
4FGL J0521.7+2112	VER J0521+211	0.108	15.20	3.44	2.83	1.94	0.37	44.15	44.67	44.86	44.65	44.60	44.31	Archambault et al. (2013)
4FGL J2158.8-3013	PKS 2155-304	0.116	15.76	3.53	2.88	1.85	−0.02	43.76	44.29	42.99	45.28	45.19	44.74	H.E.S.S. Collaboration et al. (2010b)
4FGL J1813.5+3144	B2 1811+31	0.117	15.05	4.1		2.04	0.26	43.11	43.85	43.73	44.04	43.97	43.64	Benbow & VERITAS Collaboration (2022)
4FGL J2250.0+3825	B 32247+381	0.1187	16.36	3.2	2.69	1.74	−0.01	43.90	44.42	42.96	44.16	44.01	43.60	Berger et al. (2011)
4FGL J1518.0-2731	TXS 1515-273	0.1284	15.08	3.11		2.05	0.09	44.67	45.20	44.04	45.57	44.18	43.78	Acciari et al. (2020)
4FGL J1217.9+3007	1ES 1215+303	0.131	15.21	3.6	2.61	1.93	0.36	43.12	43.64	44.98	44.28	44.66	44.37	Aliu et al. (2013)
4FGL J1230.2+2517	S3 1227+25	0.135	15.80	3.79		2.10	0.56	44.33	45.07	44.38	44.71	44.82	44.60	Acharyya et al. (2023)
4FGL J0721.9+7120	S 50716+714	0.127	14.17	3.45		2.06	0.48	44.65	45.17	45.14	45.57	45.58	45.30	Anderhub et al. (2009)
4FGL J0809.8+5218	1ES 0806+524	0.138	15.65	2.97		1.88	3.55E-03	44.43	45.29	44.69	44.49	44.38	43.94	Aleksić et al. (2015)
4FGL J1443.9-3908	PKS 1440-389	0.1385	15.65	3.7	2.18	2.10	0.13	44.12	44.86	44.41	44.85	44.39	44.02	Abdalla et al. (2020)
4FGL J0232.8+2018	1ES 0229+200	0.1396	19.05	2.5	1.44	1.77	0.91	43.65	44.39	43.70	44.15	43.84	43.23	Aharonian et al. (2007)
4FGL J2324.7-4041	1ES 2322-409	0.1736	15.76	3.4		1.76	0.16	43.93	44.66	43.36	44.69	44.60	44.24	Abdalla et al. (2019)
4FGL J2001.2+4353	TeV J2001+438	0.1739		2.8		1.98	0.04	45.31	46.05	44.76	44.96	44.91	44.46	Aleksić et al. (2014)
…	…	…	…	…	…	…	…	…	…	…	…	…	…	…
…	…	…	…	…	…	…	…	…	…	…	…	…	…	…

Note. Column (1): 4FGL name; Column (2): Other name; Column (3): redshift; Column (4): synchrotron peak frequency; Column (5): TeV observed spectral index; Column (6): TeV intrinsic spectral index; Column (7): GeV photon index; Column (8): mid-IR spectral index; Column (9): TeV observed luminosity; Column (10): TeV intrinsic luminosity; Column (11): GeV luminosity; Column (12)–(14) mid-IR luminosity at 3.4 μm, 4.6 μm and 12 μm; Column (15) references for TeV sources.

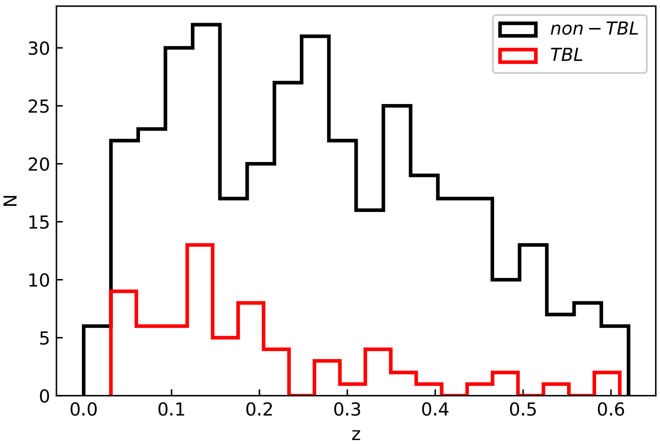

Figure 1. Histogram of redshift. Black represents 368 non-TBLs, red represents 42 TBLs.

where $I_0 = 3.45 \times 10^{-11}$, which is in units of TeV cm^{-2} s^{-1}, $\alpha_{\rm crab} = 2.63$ is the spectral photon index of the Crab Nebula (Aharonian et al. 2006). In this work, all the flux densities are converted to the units of erg cm^{-2} s^{-1} Hz^{-1}, and K-corrected by $f_\nu^{\rm res} = (1+z)^{(\alpha-1)} f_\nu^{\rm obs}$.

Luminosity can be calculated from the detected photons (Fan et al. 2012; Lin & Fan 2016; Yang et al. 2017) through

$$\nu L = 4\pi d_L^2 \nu f\,({\rm erg\ s^{-1}}) \tag{8}$$

where f is the flux density, d_L is luminosity distance which can be expressed as

$$d_L = (1+z)\cdot\frac{c}{H_0}\cdot\int_1^{1+z}\frac{1}{\sqrt{\Omega_m x^3 + 1 - \Omega_m}}dx \tag{9}$$

In this work, we calculated the monochromatic luminosity at mid-IR, i.e., 3.4 μm, 4.6 μm and 12 μm, and γ-ray at 50 GeV for the A1, and also calculated the luminosity at 1 TeV for the T1 with available TeV flux, namely the observed luminosity $\log \nu L_{\rm TeV}^{\rm obs}$. In addition, we obtained an EBL-corrected spectrum using the EBL absorption depth predicted by SAMs, and we refer to the luminosity calculated from an EBL-corrected spectrum as the intrinsic luminosity $\log \nu L_{\rm TeV}^{\rm int}$. The corresponding results are shown in the column (9)–(14) in Table 1.

3. Results

3.1. Spectral Index and Luminosity

In this paper, we used a power law ($f_\nu \propto \nu^{-\alpha}$) to describe the mid-IR continua and obtained the mid-IR spectral index $\alpha_{\rm MIR}$ for the S1. To compare TBLs and non-TBLs, we also considered the T1 and the N1 respectively. We found that the spectral index of most sources are falls in a range [0, 0.6], the median value is 0.31 for the T1 and 0.36 for the N1, and the maximum value is 1.2 for TBLs and 1.28 for non-TBLs. We obtained the average spectral index and employed a T-test for the spectral index distribution, and the results are $\langle\alpha_{\rm MIR}\rangle = 0.40 \pm 0.08$ for the whole sample, $\langle\alpha_{\rm MIR}\rangle = 0.35 \pm 0.09$ for the T1 and $\langle\alpha_{\rm MIR}\rangle = 0.41 \pm 0.08$ for the N1. When a T-test is adopted to the two values, it shows that the probability for the averaged MIR spectral index of $\langle\alpha_{\rm MIR}\rangle = 0.35 \pm 0.09$ for the T1 to be close to $\langle\alpha_{\rm MIR}\rangle = 0.41 \pm 0.08$ is p = 7.3×10^{-6} for T-test being greater than 0.05, suggesting that both distribution are from different parent distribution, and the TBLs have a more flat mid-IR spectrum than the non-TBLs. In addition, we also discussed the mid-IR spectral index considering the subclasses of the A1, i.e., LBLs, IBLs and HBLs, results are $\langle\alpha_{\rm MIR}\rangle = 0.69 \pm 0.08$ for 114 LBLs, $\langle\alpha_{\rm MIR}\rangle = 0.36 \pm 0.04$ for 172 IBLs and 0.25 ± 0.03 for 172 HBLs respectively. It is noticeable that the LBLs have greater average $\alpha_{\rm MIR}$ than HBLs, while IBLs appear to be in an interim position between LBLs and HBLs (see Figure 2).

Table 2
Average Values of Luminosity and Spectral Index

Para. (1)	Class (2)	N (3)	Ave. (4)	σ (5)	Median (6)	$p_{\rm t-test}$ (7)
$\log\nu L_{3.4\mu m}$	A1	410	44.35	0.68	44.42	
	T1	42	44.79	0.58	44.70	3.5×10^{-6}
	N1	368	44.30	0.67	44.37	
$\log\nu L_{4.6\mu m}$	A1	410	44.24	0.75	44.32	
	T1	42	44.71	0.67	44.62	8.9×10^{-6}
	N1	368	44.19	0.73	44.28	
$\log\nu L_{12\mu m}$	A1	410	43.84	0.88	44.02	
	T1	42	44.39	0.80	44.30	1.4×10^{-4}
	N1	368	43.89	0.85	44.00	
$\alpha_{\rm MIR}$	A1	410	0.40	0.08	0.35	
	T1	42	0.35	0.09	0.31	7.3×10^{-6}
	N1	368	0.41	0.08	0.36	

Note. Column (1): parameter, where L_ν denotes for the observed monochromatic luminosity at the 3.4 μm, 4.6 μm and 12 μm, respectively; Column (2): classification; Column (3): sample size (N); Column (4): averaged logarithmic value of luminosity; Column (5): 1 σ uncertainty; Column (6): median value of the logarithm of monochromatic luminosity; Column (7): T-test probability for the corresponding two distributions (p).

Monochromatic luminosities in mid-IR ($\log \nu L_{3.4\mu m}$, $\log \nu L_{4.6\mu m}$ and $\log \nu L_{12\mu m}$), γ-ray band at 50 GeV ($\log \nu L_{\rm GeV}$) and at 1 TeV ($\log \nu L_{\rm TeV}^{\rm obs}$ and $\log \nu L_{\rm TeV}^{\rm int}$) are calculated and listed in Table 1. To compare the TBLs and non-TBLs, we computed average mid-IR luminosity for the T1 and the N1, and found that average mid-IR luminosity of TBLs is higher than the non-TBLs. See Table 2 for more details.

3.2. Correlations

We applied linear regression to investigate the correlation between the mid-IR and the γ-ray bands, and obtained the following results: for the correlation between the TeV and mid-IR bands, we investigated the correlation between the TeV

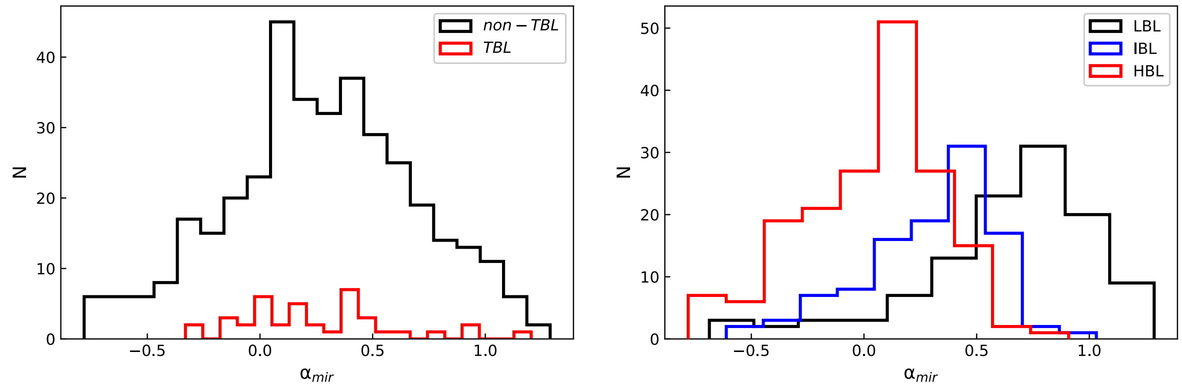

Figure 2. Histograms of the mid-IR spectral index. In the left panel, black color represents 368 non-TBLs and red color represents 42 non-TBLs; as for the right panel, subclasses of BL Lacs, i.e., LBLs, IBLs, and HBLs, are considered and represented in black, blue, and red, respectively.

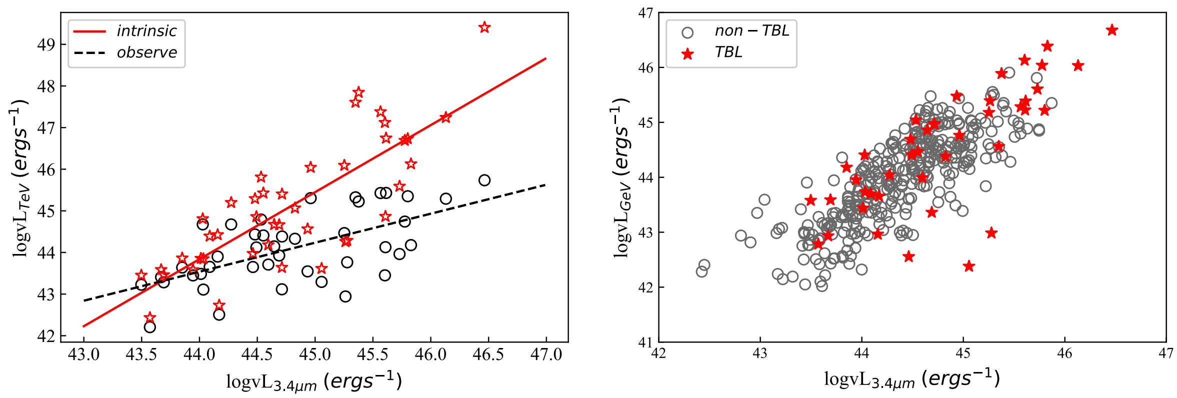

Figure 3. Plots of γ-ray luminosity against 3.4 μm luminosity. The left panel shows the correlation between the observed (black open circles) as well as the intrinsic (red open stars) luminosity at 1 TeV and the luminosity at 3.4 μm for 42 TBLs; the right panel shows the correaltion between the 50 GeV luminosity and the 3.4 μm luminosity, red stars stand for 42 TBLs, dim gray open circles stand for 368 non-TBLs.

luminosity and the mid-IR luminosity for the T1 and obtained:

$$\log \nu L_{\rm TeV}^{\rm obs} = (0.70 \pm 0.13)\log \nu L_{3.4\mu{\rm m}} + (12.88 \pm 6.25),$$

with a correlation coefficient $r = 0.62$ and a chance probability of $p < 10^{-4}$ for the observed data, and

$$\log \nu L_{\rm TeV}^{\rm int} = (1.61 \pm 0.19)\log \nu L_{3.4\mu{\rm m}} - (27.00 \pm 8.46),$$

with $r = 0.80$ and $p < 10^{-4}$ for the intrinsic data. We also conducted correlation analysis between the GeV and the mid-IR bands for A1, and we removed 10 non-TBLs with very low GeV luminosity and considered the remaining 400 BL Lacs (subset A2), which included 42 TBLs (T1) and 358 non-TBLs (subset N2). The Pearson analysis shows a significantly positive correlation between the GeV and the mid-IR bands for the A2 ($r = 0.80$, $p < 10^{-4}$). However, for a comparison between the T1 and the N2, there is no significant difference for the slope of the correlation and the correlation coefficient. The results can be seen in Table 2, and corresponding plots are shown in Figure 3 and Appendix Figure 9.

For the spectral index correlation, we studied the correlation between avaliable observed TeV spectral index and the mid-IR spectral index for 40 TBLs (subset T2). Considering that most TBLs are HBLs, we discussed 30 HBLs (subset TH1) separately. The Pearson analysis shows a positive correlation between observed TeV spectral index and mid-IR spectral index, which are $r = 0.71$, $p < 10^{-4}$ for HBLs. We obtained intrinsic TeV spectral indices of 28 TBLs (subset T3), including 22 HBLs, and performed the following analysis (see Table 3 and Figure 4). From the Figure 4 left panel, we can see 3 outliers and we removed them in our analysis. Finally, we have 25 TBLs (subset T4), which has 21 HBLs (subset TH2). In addition, we also conducted the correlation analysis between the GeV photon spectral index and the mid-IR spectral index for the A1, and also studied for the T1 and the N1 separately. The corresponding results are shown in Table 3 and plots are shown in Figure 6.

4. Discussion

An outstanding issue is that whether the IR photon field provides the seed photons for the γ-ray radiation. Two models which are widely discussed are the hot circumnuclear dust

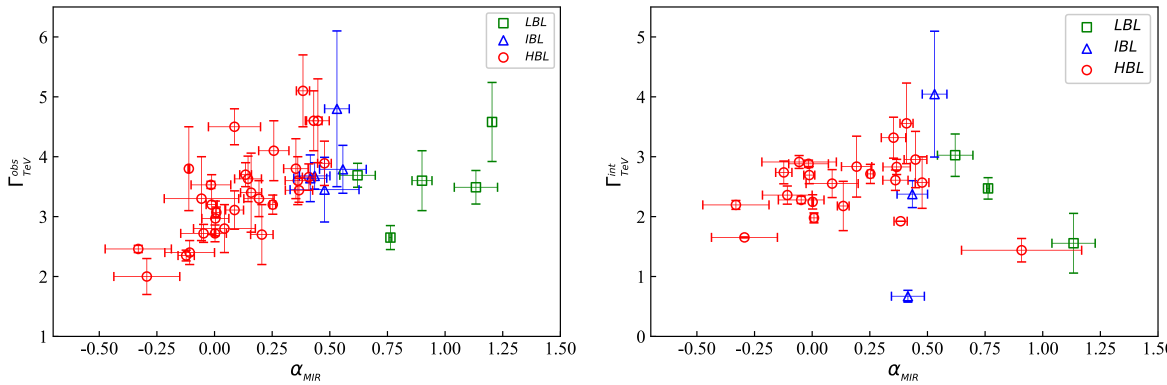

Figure 4. Plots of TeV spectral index against mid-IR spectral index. The left panel shows the TeV observed spectral indices against the mid-IR spectral indices for 40 TBLs; the right panel shows the TeV intrinsic spectral indices against the mid-IR spectral indices for 28 TBLs; red open circles, blue open triangles and green open squares stand for HBLs, IBLs and LBLs, respectively.

Table 3
Linear Correlation Fitting Results

y (1)	x (2)	Class (3)	N (4)	$a \pm \triangle a$ (5)	$b \pm \triangle b$ (6)	r (7)	p (8)
$\log \nu L^{\rm obs}_{\rm TeV}$	$\log \nu L_{3.4\mu m}$	T1	42	0.70 ± 0.13	12.88 ± 6.25	0.62	$<10^{-4}$
	$\log \nu L_{4.6\mu m}$	T1	42	0.64 ± 0.13	15.35 ± 5.84	0.61	$<10^{-4}$
	$\log \nu L_{12\mu m}$	T1	42	0.56 ± 0.12	19.33 ± 5.24	0.59	$<10^{-4}$
$\log \nu L^{\rm int}_{\rm TeV}$	$\log \nu L_{3.4\mu m}$	T1	42	1.61 ± 0.19	-27.00 ± 8.46	0.80	$<10^{-4}$
	$\log \nu L_{4.6\mu m}$	T1	42	1.47 ± 0.18	-20.66 ± 8.12	0.79	$<10^{-4}$
	$\log \nu L_{12\mu m}$	T1	42	1.29 ± 0.18	-19.02 ± 7.78	0.75	$<10^{-4}$
$\log \nu L_{\rm GeV}$	$\log \nu L_{3.4\mu m}$	A2	400	1.10 ± 0.04	-4.82 ± 1.84	0.80	$<10^{-4}$
		T1	42	1.09 ± 0.15	-4.38 ± 6.76	0.75	$<10^{-4}$
		N2	358	1.09 ± 0.04	-4.57 ± 1.93	0.80	$<10^{-4}$
$\log \nu L_{\rm GeV}$	$\log \nu L_{4.6\mu m}$	A2	400	1.00 ± 0.04	-0.43 ± 1.67	0.80	$<10^{-4}$
		T1	42	1.00 ± 0.14	-0.40 ± 6.38	0.74	$<10^{-4}$
		N2	358	1.00 ± 0.04	-0.07 ± 1.73	0.80	$<10^{-4}$
$\log \nu L_{\rm GeV}$	$\log \nu L_{12\mu m}$	A2	400	0.84 ± 0.04	6.88 ± 1.58	0.76	$<10^{-4}$
		T1	42	0.88 ± 0.14	5.47 ± 6.02	0.71	$<10^{-4}$
		N2	358	0.83 ± 0.04	7.70 ± 1.62	0.76	$<10^{-4}$
$\Gamma^{\rm obs}_{\rm TeV}$	$\alpha_{\rm MIR}$	T2	40	1.07 ± 0.8	3.19 ± 0.12	0.52	$<10^{-4}$
		TH1	30	2.41 ± 0.44	3.09 ± 0.11	0.72	$<10^{-4}$
$\Gamma^{\rm int}_{\rm TeV}$	$\alpha_{\rm MIR}$	T4	25	0.85 ± 0.33	2.47 ± 0.11	0.47	1%
		TH2	21	0.93 ± 0.38	2.46 ± 0.10	0.49	2%
$\Gamma_{\rm GeV}$	$\alpha_{\rm MIR}$	A1	410	0.21 ± 0.02	1.98 ± 0.01	0.45	$<10^{-4}$
		T1	42	0.28 ± 0.05	1.84 ± 0.02	0.65	$<10^{-4}$
		N1	368	0.21 ± 0.02	2.00 ± 0.01	0.44	$<10^{-4}$
$\triangle\Gamma_{\rm obs}$	z	T2	40	3.46 ± 0.52	0.85 ± 0.13	0.73	$<10^{-4}$
$\triangle\Gamma_{\rm int}$	z	T3	28	0.26 ± 0.86	0.54 ± 0.21	0.06	77%
$\log\nu^s_p$	$\Gamma^{\rm obs}_{\rm TeV}$	T4	36	-0.69 ± 0.27	17.86 ± 0.98	-0.39	1%
		TH3	26	-0.59 ± 0.22	18.79 ± 0.68	-0.47	1%
$\log\nu^s_p$	$\Gamma^{\rm int}_{\rm TeV}$	T5	25	-0.20 ± 0.36	16.08 ± 0.95	-0.11	59%
		TH4	19	-0.98 ± 0.40	18.55 ± 1.04	-0.59	2×10^{-4}

Note. Column (1) (2): relation; Column (3): classification: subset A series represents the whole sample, T stands for TBL, TH stands for TeV HBL and N stands for non-TBL; Column (4): sample size (N); Column (5): slope and corresponding uncertainty, $a \pm \triangle a$; Column (6): intercept and corresponding uncertainty, $b \pm \triangle b$; Column (7): correlation coefficient (r); Column (8): chance probability (p).

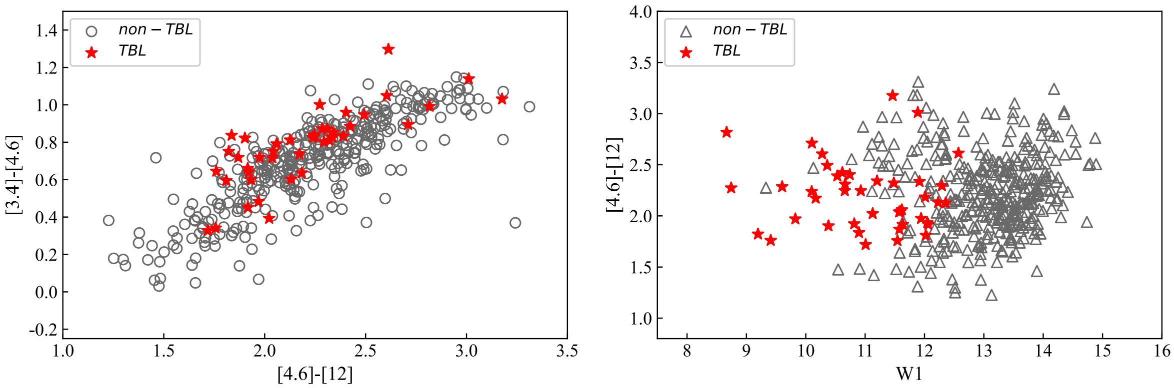

Figure 5. Plots of [3.4]–[4.6] μm against [4.6]–[12] μm colorcolor (left panel) and color-magnititue (right panel) for Fermi-WISE BL Lacs sample. We plot the 410 Fermi BL Lacs associated with a WISE source within a region of radius 2.″4. Red stars represent 42 TBLs, dim gray represents 368 non-TBLs. For the color-magnititue plot, here shows the [4.6]–[12] μm vs. W1 plot, while [3.4]–[12] μm vs. W2 and [3.4]–[4.6] μm vs. W3 are shown in Appendix.

model (Wagner et al. 1995; Xie et al. 1997) and synchrotron self-Compton models (Ghisellini & Maraschi 1989; Xie et al. 1998). However, if high and rapid variability is detected, a kpc-scale origin could be ruled out. Anjum et al. (2020) found the intraday mid-IR variability of γ-ray emitting blazars and proposed that mid-IR radiation region is in the jet. Therefore, the mid-IR emission from synchrotron radiation in the jet will probably become a soft photon field for γ-ray radiation, and an empirical correlation between the mid-IR and the γ-ray bands can be expected since they come from the same electron distribution.

4.1. Color and Magnitude

Since the WISE provides an exploration of the link between the mid-IR and the γ-ray bands. Massaro et al. (2011) and D'Abrusco et al. (2012) discovered that the γ-ray-emitting blazars occupy a distinct region in the [3.4]–[4.6] against [4.6]–[12] μm colorcolor diagrams and well separated from other extragalactic sources whose IR emission is dominated by thermal radiation, i.e., the WISE Gamma-ray Strip. Particularly, Massaro et al. (2013) found that the TBLs are more confined near the tail of the WGS and proposed new criteria for selecting TeV BL Lac candidates based on the mid-IR bands observations. In this work, we build the [3.4]–[4.6] against [4.6]–[12] μm two-dimensional colorcolor diagrams for the the T1 and N1, and the results are shown in Figure 5. We likewise found that all sources are gathered together to form the WISE Gamma-ray Strip. It can be seen that there is a certain connection between the mid-IR and the γ-ray making the Fermi-Wise BL Lacs occupy a compact region in the colorcolor diagram. TBLs and non-TBLs occupy a identical region on the [3.4]–[4.6] against [4.6]–[12] μm colorcolor diagram (see Figure 5 left panel), suggesting that it is somewhat difficult to distinguish the TBLs and the non-TBLs in [3.4]–[4.6] against [4.6]–[12] color–color diagram. We also present a color–magnitude diagram for the three WISE bands (see Figure 5 right panel and Appendix Figure 10). We can see that TBLs and non-TBLs occupy different regions, and most of TBLs appear significantly brighter than non-TBLs for similar values of the color-index. Furthermore, as seen in Figure 10 in Appendix, distribution trends of non-TBLs themselves are also different, whether it implies that some non-TBLs may have other IR components. Thanks to such IR-γ-ray connection, WISE data have been used to search for blazar-like sources within unidentified γ-ray sources (Massaro et al. 2012; D'Abrusco et al. 2014, 2019). It also sheds new light on the search for TBLs, and we look forward to more observations.

4.2. Average Values

In the IR region, three emission components must be modeled: starlight from the host galaxy, beamed jet synchrotron emission and dusty torus emission. Plotkin et al. (2012) pointed out that BL Lac objects lack observational signatures of the dusty torus in the mid-IR from WISE. This may be due to the fact that low power BL Lacs are poor accretion devices and thus the dust is poorly heated (Hardcastle et al. 2009); Anjum et al. (2020) found the intraday mid-IR variability from γ-ray emitting blazars. In this case, it is less likely that thermal dust torus emission is included in the mid-IR band of WISE; Glass (1981) found that the spectral index of BL Lacs with underlying galaxy are generally smaller than those of objects without underlying galaxy in general; Falomo et al. (1993) and Pian et al. (1994) found that the contribution of the host galaxy produces a flattening of the near-infrared energy distribution; Chen & Shan (2011) found that all spectra can be well fitted by a power-law distribution, indicating that these BL Lac objects are synchrotron emission mechanisms. In this work, we use a power-law to fit the mid-IR spectral index. From Table 2, we can see that the average mid-IR spectral index for the whole sample is 0.40 ± 0.08, and that is 0.35 ± 0.09 for TBLs and

0.41 ± 0.08 for non-TBLs, showing that the mid-IR spectrum of TBLs is more flat than that of the non-TBLs. The result is similar to the findings by Lin & Fan (2016), who obtained that the radio to optical effective spectrum index is 0.275 on average for TeV BL Lacs, and that is 0.436 for non-TeV BL Lacs, namely TeV BL Lacs have a more flat radio to optical spectral index than non-TeV BL Lacs. When the T-test is adopted to the two average values 0.35 ± 0.09 and 0.41 ± 0.08, it shows that the probability for the two average values to be close is 7.3×10^{-6}, suggesting that the two average values are different. We can say that the MIR spectrum of the TBLs is more flat than that of the non-TBLs. If we consider the subclasses of BL Lacs separately, we can get $\langle \alpha_{\rm MIR|LBL} \rangle = 0.71 \pm 0.09$, $\langle \alpha_{\rm MIR|IBL} \rangle = 0.38 \pm 0.04$, $\langle \alpha_{\rm MIR|HBL} \rangle = 0.21 \pm 0.03$ for LBLs, IBLs and HBLs respectively. There is a tendency for the mid-IR spectral index to become steeper from HBLs to LBLs, namely, $\langle \alpha_{\rm MIR|HBL} \rangle < \langle \alpha_{\rm MIR|IBL} \rangle < \langle \alpha_{\rm MIR|LBL} \rangle$, which means that HBLs have a more flat mid-IR spectrum than LBLs and IBLs. Plotkin et al. (2012) mentioned that most lower-redshift BL Lacs may be influenced by the host galaxy. Since most of the HBLs in our sample are distributed in the low redshift interval, accordingly, we suggest that TeV HBLs are likely to be influenced by host galaxies.

For the average mid-IR luminosity, both the TBLs and the non-TBLs show a trend of higher luminosity with shorter wavelengths, but the difference is that TBLs and non-TBLs really show different mid-IR luminosity with the average logarithmic luminosity in the mid-IR of TBLs being greater than that of non-TBLs, the null hypothesis can be rejected to over a 99% level of significance with a T-test, which indicates that TBLs and non-TBLs can be distinguished in the mid-IR luminosity distribution. Considering that 31 out of 42 TBLs are HBLs, a plausible explanation is that perhaps there are other mid-IR radiation components for TeV-detected HBLs, such as host galaxies, which leading to higher mid-IR luminosity.

Based on above discussions, the higher luminosity as well as the more flat spectrum in the mid-IR band could well be characteristic of TBLs. We expect a larger TeV sample and deeper observations in the mid-IR will be helpful to verify the idea.

4.3. Luminosity Versus Luminosity

Many previous studies have examined the correlation between the γ-ray and and other low energy bands for blazars (Dondi & Ghisellini 1995; Fan et al. 1998; Xie et al. 1998; Yang & Fan 2005; Lin & Fan 2016; Massaro & D'Abrusco 2016; Liodakis et al. 2018; Zhang & Fan 2018). Xie et al. (1998) found that the near-infrared band and the γ-ray band correlation was the strongest through comparison with other bands, and the variability behavior of the γ-ray and the near-IR fluxes was consistent. They thus suggested that the main γ-ray radiation mechanism is the synchrotron self-Compton process; Lin & Fan (2016) studied the correlation between radio, optical, X-ray and γ-ray bands, also compared TBLs and non-TBLs, but no discussion of the correlation between the γ-ray and the IR bands. In this work, we considered the mutual correlations between $\log \nu L_\gamma$ and $\log \nu L_{\rm MIR}$. For the correlation between the TeV band and the mid-IR bnad, the Pearson analysis shows a positive correlation between the observed TeV luminosity and the mid-IR luminosity at 3.4 μm, with $r = 0.62$ and $p < 10^{-4}$. Since very high energy (VHE, $100\,{\rm GeV} \leqslant {\rm E} < 10$ TeV) γ-ray photons can interact with EBL photons to produce electron-positron pairs during propagation, we therefore apply an EBL absorption correction for the TeV band. It is found that, after performing EBL absorption correction, the TeV luminosity and mid-IR luminosity at 3.4 μm show a more significantly positive correlation ($r = 0.80$, $p < 10^{-4}$), which is an indication that there is a certain correlation between the TeV and the mid-IR bands. We also derived a positive correlation between the GeV and the mid-IR luminosities for the A2, and the GeV and the mid-IR luminosities of non-TBLs are more closely correlated than that of the TBLs. In addition, we compared the mid-IR band and two γ-ray bands (GeV and TeV) luminosities correlations for the T1 and found that the GeV and the mid-IR bands are more closely correlated than that between the TeV and the mid-IR bands, and show a tendency that the shorter the mid-IR wavelength, the better the correlation. To sum up, we suggest that higher-energy mid-IR photons are probably scattered by relativistic electrons up to the γ-ray band, even up to TeV band, and this possibility increases with shorter IR wavelengths.

Variability is one of observational properties of blazars. It is detected over the whole electromagnetic wave bands with timescales from minutes to years (Fan et al. 2005). The variability timescales shed lights on the emission size and even constrain the central black hole masses. Many TBLs are detected during their flare state of the γ-ray (Punch et al. 1992; Quinn et al. 1996; Catanese et al. 1998; Chadwick et al. 1999; Shukla & Mannheim 2020; Tolamatti et al. 2022; Wang et al. 2022). The variability in different wavelength can be used to investigate the emission mechanism. For TBLs, we can study the TeV emission mechanism by investigating the variability between the low energy band and the TeV band. If the TeV emissions in blazars are from the up-scattered MIR photons, then there is a correlation between the MIR flare and the TeV flares. In this case, if a flare is detected in the MIR bands, then one can expect a flare in the TeV band. Therefore, we can expect TeV BL Lac candidates by investigating the MIR flare of BL Lacs. This is perhaps an interesting work in the future. If we can monitor the the MIR band and TeV band, then we can study the flare properties between the two bands and constrain the emission region size, the central black hole masses and even the TeV emission mechanism.

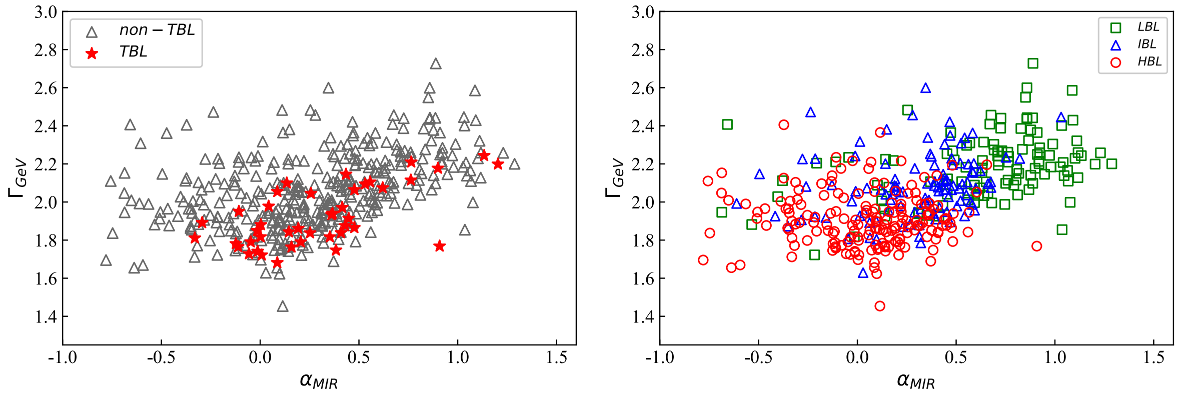

Figure 6. Plots of GeV spectral index against mid-IR spectral index. The left panel shows the difference between TBLs and non-TBLs, with red stars standing for 42 TBLs and dim gray open triangles for 354 non-TBLs; the right panel shows the difference between IBLs, IBLs and HBLs, green open squares for IBLs, blue open triangles for IBLs and red open circles for HBLs.

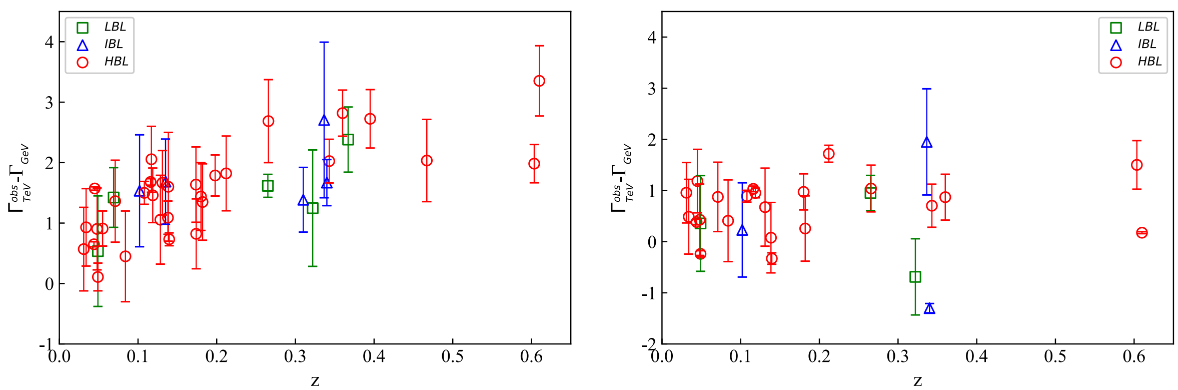

Figure 7. Plots of EBL attenuation aganist redshift. The left panel shows the relationship between observed EBL attenuation and redshift, and the right panel shows intrinsic EBL attenuation and redshift.

4.4. Other Correlations

For the correlation between the γ-ray and the mid-IR spectral indices, D'Abrusco et al. (2012) found a positive correlation between $\Gamma_{\rm GeV}$ and $\alpha_{\rm MIR}$ for blazars, and the correlation is dominated by the BL Lacs. In our work, $\Gamma_{\rm GeV}$ and $\alpha_{\rm MIR}$ show a weak correlation with $r = 0.45$ and $p < 10^{-4}$, and we also found that D'Abrusco et al. (2012) gave $r = 0.59$. When we considered the TBLs and the non-TBLs separately, it is found that TBLs possess a closer correlation than the non-TBLs in the $\Gamma_{\rm GeV}$-$\alpha_{\rm MIR}$ correlation, which is $r = 0.65$ for the TBLs and $r = 0.44$ for the non-TBLs. Furthermore, when considering the subclasses of BL Lacs, there is a gradual softening trend from HBLs to LBLs (see Figure 6). For the correlation analysis between the observed TeV spectral index and mid-IR spectral, we obtained a positive correlation ($r = 0.72$ and $p < 10^{-4}$) for the TH1. There is no significant correlation between the intrinsic TeV spectral index and the mid-IR spectral index. The results are shown in Table 3 and Figure 4.

Since the $\Gamma_{\rm TeV}$ is influenced by the EBL absorption as proposed by Stecker & Scully (2006, 2010), then a simple linear correlation $\triangle\Gamma_{\rm obs} = \alpha\, z + \beta$, can be used to characterize the EBL absorption effect on the observed spectral break. The observed spectral break $\triangle\Gamma_{\rm obs}$ could be represented as the discrepancy between the observed VHE and HE spectral indices, i.e., $\triangle\Gamma_{\rm obs} = \Gamma_{\rm TeV,obs}$ - $\Gamma_{\rm GeV,obs}$. As the break induced by EBL should be linearly correlated the redshift, then we can obtain a relationship with $\triangle\Gamma_{\rm EBL}(E,z) = \alpha\, z$. In this sense, we can obtain a relationship between the observed spectral break and redshift: $\triangle\Gamma_{\rm obs} = \Gamma_{\rm TeV,obs}$-$\Gamma_{\rm GeV,obs} = \alpha\, z$+$\beta$, β represents the intrinsic curvature (Zhong et al. 2018). In most cases, the attenuation of the spectrum occurs beyond 100 GeV (Zheng & Kang 2013; Zheng et al. 2016), and therefore the observed HE spectral index is equal to the intrinsic HE spectral index (i.e., $\Gamma_{\rm GeV,int} = \Gamma_{\rm GeV,obs}$). We thus get a relation, that is $\triangle\Gamma_{\rm int} = \Gamma_{\rm TeV,int}$-$\Gamma_{\rm GeV} = \alpha\, z$+$\beta$. The results are shown in Table 2 and Figure 7. In the range of redshifts from 0.031 to 0.61, the observed data and redshift show a positive correlation ($r = 0.73$

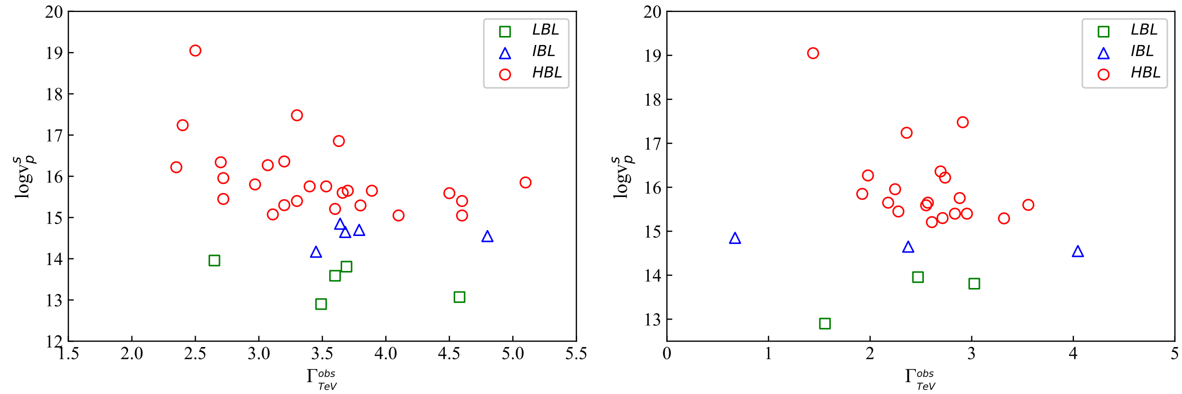

Figure 8. Plots of synchrotron peak frequency against TeV spectral index. The left panel shows synchrotron peak frequency against observed TeV spectral index for 36 TBLs; the left panel shows synchrotron peak frequency against intrinsic TeV spectral index for 25 TBLs; green open squares for IBLs, blue open triangles for IBLs and red open circles for HBLs.

and $p < 10^{-4}$) for the T2, and as for the intrinsic data, there is no correlation for the T3. The results show that the observed TeV spectral index is affected by the EBL absorption, which is consistent with that by Zhong et al. (2018).

By cross-checking the latest 4LAC catalog (Ajello et al. 2022) and Yang et al. (2023), among the 42 TBLs, we obtained 36 TBLs (subset T4) with both the observed TeV spectral index and the synchrotron peak frequency, and 26 TBLs (subset T5) with both the intrinsic TeV spectral index and the synchrotron peak frequency. We found a weak negative correlation between the intrinsic TeV spectral index and the mid-IR spectral index of HBLs, with $r = –0.59$ and $p = 2 \times 10^{-4}$, which implies that for HBLs, the higher peak frequency will have a harder TeV spectrum. The corresponding results are shown in Table 3 and plots are shown in Figure 8.

From the above discussions, there is a correlation between the TeV spectral index and the mid-IR spectralfrom index of HBLs, and a correlation between the TeV luminosity and the MIR luminosity, which is consistent with the expectations of the SSC model. But it may be influenced by the EBL absorption. The mid-IR photons from HBLs with extreme relativistic electrons are likely to be scattered to the TeV band. Since the limited number of TeV sources and their WISE counterparts, we still need a larger TeV sample and sufficient infrared data for further study.

5. Conclusions

In this paper, we compiled a sample of 410 BL Lacs by cross-matching the WISE catalog with the Fermi-LAT catalog, as well as considering the band sensitivity of the WISE detection and the redshift range. We also collected the energy spectrum information of TeV-detected BL Lacs from TeVcat and references, and calculated the monochromatic luminosities at the mid-IR, GeV and TeV bands and fitted the mid-IR spectral index. Besides, the EBL correction was done for the observed TeV luminosity. We performed some statistical correlation analysis for the important parameters. Our conclusions are summarized as follows:

1. Our sample forms a WISE-Gamma Strip in the [3.4]–[4.6]–[12] μm color–color diagram. It is the connection between the γ-rays and the mid-IR bands which enables the Fermi-WISE BL Lacs occupy a compact region in the color–color diagram. For the color-magnititue diagram, TBLs are brighter than non-TBLs at similar color-index.
2. TBLs exhibit higher mid-IR luminosity, and the average mid-IR spectral index of TBLs is smaller than that of non-TBLs. The mid-IR spectrum of HBLs is more flat than that of LBLs and IBLs, showing a trend, i.e., $\langle\alpha_{\mathrm{MIR|HBL}}\rangle < \langle\alpha_{\mathrm{MIR|IBL}}\rangle < \langle\alpha_{\mathrm{MIR|LBL}}\rangle$.
3. The mid-IR luminosity is positively correlated with the GeV luminosity and the intrinsic TeV luminosity, which is consistent with the expectations of the SSC model.
4. The TBLs show a stronger positive correlation than non-TBLs in Γ_{GeV}-α_{MIR} spectral index correlation. The mid-IR spectral index is positively correlated with the observed TeV spectral index for TeV HBLs.
5. The intrinsic TeV spectral index and the synchrotron peak frequency show a weak negative correlation tendency for HBLs, we suggest that HBLs with extreme relativistic electrons are more likely to scatter mid-IR photons up to the TeV band.

Acknowledgments

We thank the anonymous reviewers for the constructive suggestions and comments! The work is partially supported by the National Natural Science Foundation of China (NSFC U2031201, NSFC 11733001, U2031112), Guangdong Major Project of Basic and Applied Basic Research (grant No. 2019B030302001). Z.Y. Pei acknowledges support from National Science Foundation for Young Scientists of China (grant 12103012). X.H. Ye would like to thank the financial support from the China Scholarship Council (202208440164). We also acknowledge the science research grants from the China Manned Space Project with No. CMS-CSST-2021-A06, and the supports for Astrophysics Key Subjects of Guangdong Province and Guangzhou City. Scientific and Technological Cooperation Projects (2020-2023) between the People's Republic of China and the Republic of Bulgaria.

Appendix

In this Appendix, we present additional plots, i.e., $\log \nu L_{\gamma}$-$\log \nu L_{\rm MIR}$ diagrams (see Figure 9) and color–magnitude diagrams (see Figure 10).

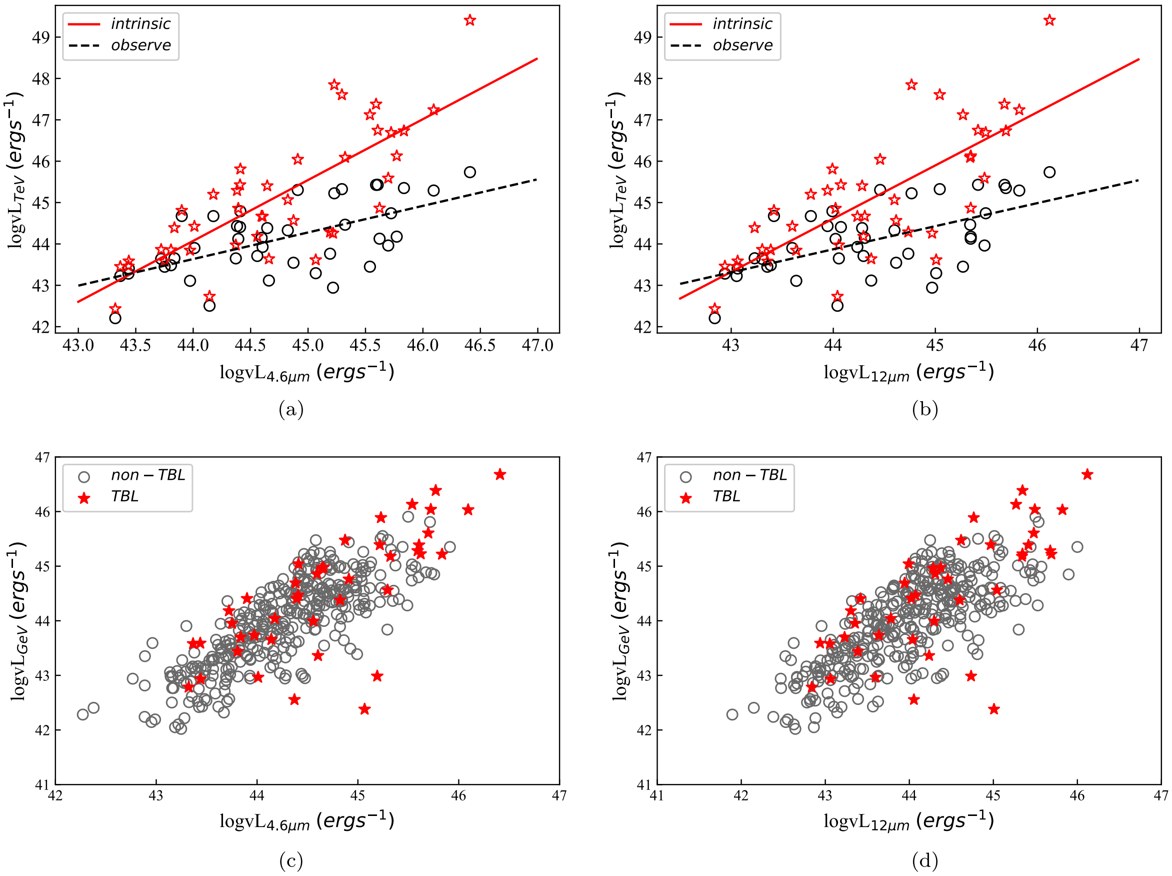

Figure 9. Plots of γ-ray luminosity against mid-IR luminosity. (a) and (b) shows the correlation between the observed (black open circles) as well as the intrinsic (red open stars) luminosity at 1 TeV and the luminosity at 4.6 μm and 12 μm for 42 TBLs; (c) and (d) shows the correaltion between the 50 GeV luminosity and the 4.6 and 12 μm luminosity, red stars stand for 42 TBLs, dim gray open circles stand for 368 non-TBLs.

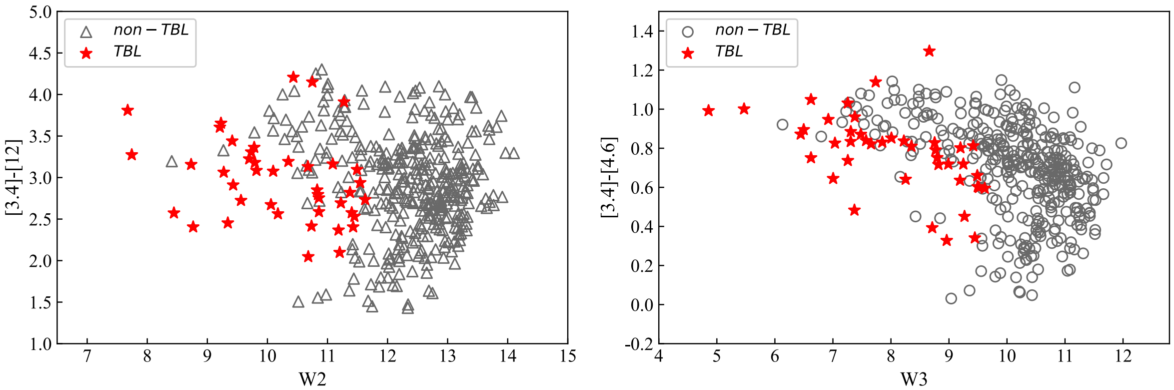

Figure 10. Plots of color-magnititue for Fermi-WISE BL Lacs sample. Right panel shows [3.4]–[12] μm vs. W2 and left panel shows [3.4]–[4.6] μm vs. W3. Red stars represent 42 TBLs, dim gray circle represents 368 non-TBLs.

ORCID iDs

Jingchao Liang https://orcid.org/0000-0003-1077-1872
Xiangtao Zeng https://orcid.org/0000-0002-0551-5615
Jingtian Zhu https://orcid.org/0000-0002-8206-5080
Hubing Xiao https://orcid.org/0000-0001-8244-1229
Zhiyuan Pei https://orcid.org/0000-0002-4970-3108
Junhui Fan https://orcid.org/0000-0002-5929-0968

References

Abdalla, H., Aharonian, F., Ait Benkhali, F., et al. 2019, MNRAS, 482, 3011
Abdalla, H., Adam, R., Aharonian, F., et al. 2020, MNRAS, 494, 5590
Abdo, A. A., Ackermann, M., Agudo, I., et al. 2010, ApJ, 716, 30
Abdo, A. A., Ackermann, M., Ajello, M., et al. 2009, ApJ, 700, 597
Abdollahi, S., Acero, F., Ackermann, M., et al. 2020, ApJS, 247, 33
Abdollahi, S., Acero, F., Baldini, L., et al. 2022, ApJS, 260, 53
Acciari, V. A., Aliu, E., Aune, T., et al. 2009, ApJ, 707, 612
Acciari, V. A., Ansoldi, S., Antonelli, L. A., et al. 2020, ApJS, 247, 16
Acciari, V. A., Arlen, T., Aune, T., et al. 2011, ApJ, 729, 2
Acero, F., Ackermann, M., Ajello, M., et al. 2015, ApJS, 218, 23
Acharyya, A., Adams, C., Archer, A., et al. 2023, ApJ, 950, 152
Ackermann, M., Ajello, M., Allafort, A., et al. 2011, ApJ, 741, 30
Aharonian, F., Akhperjanian, A. G., Barres de Almeida, U., et al. 2007, A&A, 475, L9
Aharonian, F., Akhperjanian, A. G., Bazer-Bachi, A. R., et al. 2006, A&A, 457, 899
Aharonian, F. A. 2000, NewA, 5, 377
Ahnen, M. L., Ansoldi, S., Antonelli, L. A., et al. 2017, MNRAS, 468, 1534
Ajello, M., Baldini, L., Ballet, J., et al. 2022, ApJS, 263, 24
Albert, J., Aliu, E., Anderhub, H., et al. 2006a, ApJL, 648, L105
Albert, J., Aliu, E., Anderhub, H., et al. 2006b, ApJ, 639, 761
Albert, J., Aliu, E., Anderhub, H., et al. 2007a, ApJ, 663, 125
Albert, J., Aliu, E., Anderhub, H., et al. 2007b, ApJL, 666, L17
Aleksić, J., Ansoldi, S., Antonelli, L. A., et al. 2014, A&A, 572, A121
Aleksić, J., Ansoldi, S., Antonelli, L. A., et al. 2015, MNRAS, 451, 739
Aliu, E., Archambault, S., Arlen, T., et al. 2013, ApJ, 779, 92
Allen, C., Archambault, S., Archer, A., et al. 2017, MNRAS, 471, 2117
Anderhub, H., Antonelli, L. A., Antoranz, P., et al. 2009, ApJL, 704, L129
Anjum, A., Stalin, C. S., Rakshit, S., Gudennavar, S. B., & Durgapal, A. 2020, MNRAS, 494, 764
Archambault, S., Arlen, T., Aune, T., et al. 2013, ApJ, 776, 69
Atwood, W. B., Abdo, A. A., Ackermann, M., et al. 2009, ApJ, 697, 1071
Begelman, M. C., & Sikora, M. 1987, ApJ, 322, 650
Benbow, W. & VERITAS Collaboration 2022, ICRC, 37, 794
Berger, K., Giavitto, G., Lindfors, E., et al. 2011, arXiv:1110.6368
Blandford, R. D., & Rees, M. J. 1978, in BL Lac Objects, ed. A. M. Wolfe (Pittsburgh, PA: Univ. Pittsburgh), 328
Cai, J. T., Kurtanidze, S. O., Liu, Y., et al. 2022, ApJS, 260, 47
Catanese, M., Akerlof, C. W., Badran, H. M., et al. 1998, ApJ, 501, 616
Chadwick, P. M., Lyons, K., McComb, T. J. L., et al. 1999, ApJ, 513, 161
Chen, P. S., Fu, H. W., & Gao, Y. F. 2005, NewA, 11, 27
Chen, P. S., & Shan, H. G. 2011, ApJ, 732, 22
Costamante, L., & Ghisellini, G. 2002, A&A, 384, 56
D'Abrusco, R., Álvarez Crespo, N., Massaro, F., et al. 2019, ApJS, 242, 4
D'Abrusco, R., Massaro, F., Ajello, M., et al. 2012, ApJ, 748, 68
D'Abrusco, R., Massaro, F., Paggi, A., et al. 2014, ApJS, 215, 14
Deng, J. H., Hu, S. M., Jiang, Z. J., Xiang, Y. C., & Zhou, R. X. 2022, Ap&SS, 367, 43
Dondi, L., & Ghisellini, G. 1995, MNRAS, 273, 583
Falomo, R., Treves, A., Chiappetti, L., et al. 1993, ApJ, 402, 532
Fan, J. H. 2000, A&A, 358, 841
Fan, J. H., Adam, G., Xie, G. Z., et al. 1998, A&A, 338, 27
Fan, J. H., Kurtanidze, S. O., Liu, Y., et al. 2021, ApJS, 253, 10
Fan, J.-H., Romero, G. E., Wang, Y.-X., & Zhang, J.-S. 2005, ChJAA, 5, 457
Fan, J. H., Yang, J. H., Liu, Y., et al. 2016, ApJS, 226, 20
Fan, J. H., Yang, J. H., Yuan, Y. H., Wang, J., & Gao, Y. 2012, ApJ, 761, 125
Fossati, G., Maraschi, L., Celotti, A., Comastri, A., & Ghisellini, G. 1998, MNRAS, 299, 433
Ghisellini, G., & Maraschi, L. 1989, ApJ, 340, 181
Gilmore, R. C., Somerville, R. S., Primack, J. R., & Domínguez, A. 2012, MNRAS, 422, 3189
Glass, I. S. 1981, MNRAS, 194, 795
Hardcastle, M. J., Evans, D. A., & Croston, J. H. 2009, MNRAS, 396, 1929
H. E. S. S. Collaboration, Acero, F., Aharonian, F., et al. 2010a, A&A, 511, A52
H. E. S. S. Collaboration, Abramowski, A., Acero, F., et al. 2010b, A&A, 520, A83
Impey, C. D., Brand, P. W. J. L., Wolstencroft, R. D., & Williams, P. M. 1982, MNRAS, 200, 19
Konigl, A. 1981, ApJ, 243, 700
Lin, C., & Fan, J.-H. 2016, RAA, 16, 103
Liodakis, I., Romani, R. W., Filippenko, A. V., et al. 2018, MNRAS, 480, 5517
Mainzer, A., Grav, T., Bauer, J., et al. 2011, ApJ, 743, 156
Marscher, A. P., & Gear, W. K. 1985, ApJ, 298, 114
Massaro, F., & D'Abrusco, R. 2016, ApJ, 827, 67
Massaro, F., D'Abrusco, R., Ajello, M., Grindlay, J. E., & Smith, H. A. 2011, ApJL, 740, L48
Massaro, F., D'Abrusco, R., Tosti, G., et al. 2012, ApJ, 750, 138
Massaro, F., Paggi, A., Errando, M., et al. 2013, ApJS, 207, 16
Melia, F., & Konigl, A. 1989, ApJ, 340, 162
Padovani, P., Alexander, D. M., Assef, R. J., et al. 2017, A&Ar, 25, 2
Pei, Z., Fan, J., Yang, J., Huang, D., & Li, Z. 2022, ApJ, 925, 97

Pian, E., Falomo, R., Scarpa, R., & Treves, A. 1994, ApJ, 432, 547
Plotkin, R. M., Anderson, S. F., Brandt, W. N., et al. 2012, ApJL, 745, L27
Prandini, E., & Ghisellini, G. 2022, Galaxies, 10, 35
Punch, M., Akerlof, C. W., Cawley, M. F., et al. 1992, Natur, 358, 477
Planck Collaboration, Aghanim, N., Akrami, y., et al. 2020, A&A, 641, A6
Quinn, J., Akerlof, C. W., Biller, S., et al. 1996, ApJL, 456, L83
Shukla, A., & Mannheim, K. 2020, NatCo, 11, 4176
Singal, J. 2015, MNRAS, 454, 115
Stecker, F. W., & Scully, S. T. 2006, ApJL, 652, L9
Stecker, F. W., & Scully, S. T. 2010, ApJL, 709, L124
Tolamatti, A., Ghosal, B., Singh, K. K., et al. 2022, APh, 139, 102687
Urry, C. M., & Padovani, P. 1995, PASP, 107, 803
Wagner, S. J., Camenzind, M., Dreissigacker, O., et al. 1995, A&A, 298, 688
Wang, G., Fan, J., Xiao, H., & Cai, J. 2022, PASP, 134, 104101
Wills, B. J., Wills, D., Breger, M., Antonucci, R. R. J., & Barvainis, R. 1992, ApJ, 398, 454
Wright, E. L., Eisenhardt, P. R. M., Mainzer, A. K., et al. 2010, AJ, 140, 1868
Xiao, H., Fan, J., Yang, J., et al. 2019, scpma, 62, 129811
Xiao, H. B., Zhu, J. T., Fan, J. H., et al. 2022, MNRAS, 517, 4202
Xie, G. Z., Zhang, X., Bai, J. M., & Xie, Z. H. 1998, ApJ, 508, 180
Xie, G. Z., Zhang, Y. H., & Fan, J. H. 1997, ApJ, 477, 114
Yang, J., Fan, J., Liu, Y., et al. 2022a, APJ, 262, 18
Yang, W. X., Wang, H. G., Liu, Y., et al. 2022b, ApJ, 925, 120
Yang, J., Fan, J., Liu, Y., et al. 2023, SCPMA, 66, 249511
Yang, J.-H., & Fan, J.-H. 2005, ChJAA, 5, 229
Yang, J. H., Fan, J. H., Liu, Y., et al. 2017, Ap&SS, 362, 219
Ye, X. H., Zeng, X. T., Yang, W. X., et al. 2021, Ap&SS, 366, 110
Zeng, X., Zhang, Z., Pei, Z., Xiao, H., & Fan, J. 2022, Ap&SS, 367, 36
Zhang, L., Chen, S., Xiao, H., Cai, J., & Fan, J. 2020, ApJ, 897, 10
Zhang, L. X., & Fan, J. H. 2018, Ap&SS, 363, 142
Zhang, L. X., Liu, Y., & Fan, J. 2022a, ApJ, 935, 4
Zhang, Z., Zeng, X., Pei, Z., et al. 2022b, PASP, 134, 064101
Zhang, Y. H., & Xie, G. Z. 1997, A&A, 317, 393
Zheng, Y. G., & Kang, T. 2013, ApJ, 764, 113
Zheng, Y. G., Yang, C. Y., & Kang, S. J. 2016, A&A, 585, A8
Zhong, W., Liu, W. G., & Zheng, Y. G. 2018, Ap&SS, 363, 179